Revising the role of chromium on the surface of perovskite electrodes: poison or promoter for the solid oxide electrolysis cell performance ?

Dingkai Chen,[a] Basma Mewafy,[a] Fotios Paloukis,[a,b] Liping Zhong[a], Vasiliki Papaefthimiou[a], Thierry Dintzer[a], Kalliopi M. Papazisi,[c] Stella P. Balomenou,[c] Dimitrios Tsiplakides,[c,d] Detre Teschner,[e,f] Virginia Pérez-Dieste,[g] Carlos Escudero,[g] and Spyridon Zafeiratos,[a,*]

[a]*Institut de Chimie et Procédés pour l'Energie, l'Environnement et la Santé, UMR 7515 du CNRS-UdS 25 Rue Becquerel, 67087 Strasbourg, France*
[b]*Foundation for Research and Technology, Institute of Chemical Engineering Sciences (FORTH/ICE-HT), Patras, GR-26504, Greece*
[c]*Chemical Process and Energy Resources Institute /CERTH, 6th km Charilaou-Thermi Rd., 57001 Thessaloniki, Greece*
[d]*Department of Chemistry, Aristotle University of Thessaloniki, 54124 Thessaloniki, Greece*
[e]*Department of Inorganic Chemistry, Fritz-Haber-Institut der Max-Planck-Gesellschaft, Faradayweg 4-6, 14195 Berlin, Germany*
[f]*Department of Heterogeneous Reactions, Max-Planck-Institut für Chemische Energiekonversion, Stiftstrasse 34-36, 45470 Mülheim a. d. Ruhr, Germany*
[g]*ALBA Synchrotron Light Source, Carrer de la Llum 2-26, Cerdanyola del Vallès, 08290 Barcelona, Spain*

Abstract

Perovskite materials are typically used as oxygen electrodes of solid oxide fuel and electrolysis cells (SOC). The high stability of the perovskite structure in oxidative environments makes it a good candidate as a cathode electrode for steam electrolysis SOC as well. In this work, we investigate SOC with $La_{0.75}Sr_{0.25}Cr_{0.9}Fe_{0.1}O_3$ perovskite cathodes employing near ambient pressure X-ray photoelectron and near-edge X-ray absorption fine structure spectroscopies combined with online electrical measurements. Based on operando experimental evidences the surface state of the perovskite electrode is directly associated with the electrocatalytic performance of the cell. The results indicate that under steam electrolysis operating conditions the well-known Sr surface enrichment is accompanied by Cr segregation and formation of $SrCrO_4$-like oxide. In contrast to the common perception of the role of surface chromites, we show here that its presence does not induce cell deactivation, but on the contrary, is beneficial for cell performance.

Keywords: solid oxide electrochemical cells, stem electrolysis, perovskite electrodes, exsolution, near ambient pressure XPS, hydrogen production, deactivation.

1. Introduction

Solid oxide electrolysis cells (SOECs) are electrochemical devices where electrical power is converted into chemical energy in the form of fuels such as H_2 or syngas ($CO+H_2$). The high operating

temperature of SOECs, in the range of about 800 °C, leads to a significant reduction of the cell voltage, and thus to increased efficiency as compared to low-temperature electrochemical conversion devices. Besides, SOECs electrodes do not require the use of expensive and rare precious metal catalysts, which might be critical for the long-term commercialization of electrochemical converters. A typical SOEC is composed of an ion or proton conducting electrolyte, interposed between the cathode (fuel) and anode (oxygen) electrodes. Yttria-stabilized zirconia (YSZ) is the most widely used electrolyte, while metal-ceramic mixtures (cermet) and perovskite-type materials are usually employed for fuel and oxygen electrodes, respectively [1,2]. SOECs devices have high flexibility and can also operate reversibly as fuel cell systems, for example during night time to generate power by converting stored H_2. On the downside, a critical issue that hinders commercialization of SOECs is associated with degradation issues [3,4]. A particular challenge, especially in case of reversible solid oxide cells, is the lack of fuel electrodes that can operate in various atmospheres with high efficiency and stability [5].

Perovskite-based oxides offer high flexibility in their structure which constitutes them an attractive candidate for electrodes able to operate both in fuel cell and electrolysis operation mode [6]. The chemical formula of an ideal perovskite-type oxide is ABO_3, with A-site cation surrounded by 12 oxygen ions while the B-site by 6 oxygen ions. Besides, the perovskites crystal can be readily doped with aliovalent cations with different ionic radius, which may deform its structure and create different types of point defects. The most extensively used perovskite electrode is lanthanum strontium manganite ($La_{1-x}Sr_xMnO_3$ or LSM), as an oxygen electrode, due to its high stability in oxidizing atmospheres, its sufficient electrical conductivity and the thermal expansion coefficient matching the one of YSZ electrolyte. However, the absence of oxygen vacancies in LSM results in conductivities that are almost purely electronic, therefore appropriate doping or replacement of Mn sites in the perovskite structure is used in order to convert them into mixed ionic and electronic conductors (MIEC).

Apart from their use as oxygen electrodes, MIEC perovskites can be efficient fuel electrodes with comparable electrochemical performance to Ni/YSZ cermets as first demonstrated by Irvine and co-workers [7,8]. Furthermore the use of perovskite instead of cermet electrodes facilitates the stack design since perovskites are potentially redox stable and therefore can operate under 100% steam, without co-feed of H_2. Therefore, recently several types of perovskite materials have been developed and evaluated as fuel electrodes for steam and CO_2 co-electrolysis [6]. Among them, doped-lanthanum chromites show one of the highest efficiencies and stable performances during both H_2O electrolysis and H_2O-CO_2 co-electrolysis [8–10]. While initial works mostly focus on optimizing the perovskite crystal structure, in recent years the surface chemistry of the electrodes has gained

importance since can have a dramatic impact on the performance [6,11–14]. In particular, both A- and B-site cations may leave their sites in perovskite crystal and segregate to the surface region, leading to the formation of secondary phases in the form of nanoparticles. Typically oxidizing atmospheres promote surface segregation of A-site cations while in reducing environments B-site segregation (also referred to as exsolution) appears more favourable [12].

Here we report an operando NAP-XPS and NEXAFS study of porous $La_{0.75}Sr_{0.25}Cr_{0.9}Fe_{0.1}O_3$ perovskite electrodes under steam electrolysis conditions. We show that aside from the well-known surface segregation of Sr cations (A-sites), Cr segregation (B-site) can also take place under oxidation and steam electrolysis conditions. Notably, this is accompanied by a change in the Cr valence from Cr^{3+} to Cr^{6+}. A remarkable finding of this work is that the formation of Cr^{6+} species on the surface of the LSCrF electrode is not detrimental for the steam electrolysis performance, but on the contrary, may improve the electrode conductivity and the reaction kinetics.

2. Experimental Section

Sample preparation and morphology characterization

For the combined spectroscopic/electrochemical analysis two-electrode miniature electrochemical cells were prepared, consisting of an Yttria-Stabilized-Zirconia (YSZ) electrolyte sandwiched between perovskite (working) and Pt (counter) electrodes. In particular, $La_{0.75}Sr_{0.25}Cr_{0.9}Fe_{0.1}O_3$ perovskites (hereafter abbreviated as LSCrF) were synthesized using a previously reported method [15] and formed as inks (solids content 70 % *wt.*). They were thereafter applied on a 150 μm YSZ pellet (Kerafol, 8YSZ) by means of screen printing (STV, mesh 40 μm), following a typical preparation procedure for solid oxide button cells [16]. The mean electrodes' thickness was about 40 μm as estimated by cross-sectional SEM images. Before being introduced in the NAP-XPS chamber, the electrodes were calcined in air at 1200 °C for 3 h. The Pt counter electrode was painted at the opposite side of the cell using platinum paste (ESL, 542-DG). The cell was fired once more at 600 °C in air in order to remove organic residuals of the platinum paste. Platinum was chosen as counter electrode due to its known performance stability in oxidizing and reducing environments [17]. The surface morphology was inspected by SEM using a Zeiss GeminiSEM 500 microscope. Energy-dispersive X-ray spectroscopy (EDXS) mapping was combined with the SEM images to resolve the different elements on the surface of the electrodes.

Synchrotron-based experiments

Operando near ambient pressure X-ray photoelectron and near-edge absorption fine structure spectroscopies (NAP-XPS and NEXAFS, respectively) were carried out at two different end-stations at the CIRCE [18] and ISISS [19] beamlines at ALBA (Barcelona) and BESSY (Berlin)

synchrotron radiation facilities, respectively. Both setups were equipped with a SPECS Phoibos 150-NAP electron analyzer. Cells were mounted between two stainless steel clamps and gold wires were acting as the current collectors (please refer to fig. S1 in the supporting information for more details on the maunting and dimensions of the cell). Heating was performed from the rear side using an IR-laser, while the temperature was monitored at the centre of the working electrode using a recalibrated pyrometer. The gas flows into the analysis chamber were regulated either by leak valves (ALBA) or by calibrated mass flow controllers (BESSY) and monitored by a quadrupole mass spectrometer. Current flow was applied between the working and the counter electrodes and the potential were measured using a computer-controlled VersaSTAT3-200 potentiostat/galvanostat (Princeton Applied Research). The working electrode was grounded in order to avoid electrostatic charging problems. Initial annealing of the cells in 0.5 mbar O_2 was used prior to spectroscopic measurements to eliminate residual carbon from the surface. After this procedure the C 1s signal was within the noise level during all experiments. Unless otherwise stated, the total pressure during the electrochemical experiments was kept constant at 1 mbar. No significant electrostatic charging was observed under the working temperature and pressure conditions. NAP-XPS spectra were collected using selected photon energies, so that the obtained photoelectrons have the same kinetic energy (KE = 190 eV or 595 eV) and thus similar sample information depths. Please note that the angle between the surface normal and the analyzer in CIRCE and ISISS end-stations is different (50 degrees for CIRCE and 0 degrees for ISISS end-station). This influences the information depth in each set of measurements, which for KE=190 is estimated around 1.3 and 2 nm for CIRCE and ISISS end-stations, respectively. Details regarding the estimation of the information depth are given in supporting information 2, while more information about quantification of the XPS measurements can be found in a previous publications.[20–22] The peak areas were estimated after subtraction of a Shirley background and the quantitative calculations were performed based on the peak areas of La 3d, Sr 3d, Fe 2p and Cr 2p photoelectron peaks, taking into account the photo-ionization cross-sections dependence of the atomic subshells [23]. It is worth mentioning that the absolute values of the elemental atomic concentrations obtained by this approach are approximative due to the complex sample morphology, however, it is safe to compare relative values between different measurements. For the Sr 3d peak fitting we used two Sr 3d doublets with a fixed width, peak area ratio, and spin-orbit splitting, while for Cr 2p the peak profile of reference spectra was used for Cr^{3+} and a symmetric 65% Gaussian-35% Lorentzian peak for Cr^{6+} components. Photon beam damage effects were tested by shifting the analysis spot to a new sample position and the lack of differences in the spectra manifests the stability of the samples under the photon beam in the time frame of the experiment. The NEXAFS spectra were recorded in the Total Electron Yield mode (TEY-NEXAFS),

enhanced by additional electrons created by ionization of the gas phase above the sample. The estimated information depth of NEXAFS measurements is about 5 nm [24]. The theoretical $L_{2,3}$-edge spectra were calculated using the charge-transfer multiplet (CTM) approach [25,26] The calculations were done using the CTM4XAS vs 5.5 program [27] and literature values were used as guides for the Slater integrals (F_{dd}, F_{pd}, G_{pd}), the spin-orbit spitting parameter (SO), the difference between the core hole potential U_{pd} and the 3d-3d repulsion energy U_{dd}, as well as for the hopping parameters (e_g and t_{2g}) [28]. The octahedral symmetry is chosen for the calculations of both Cr^{3+} and Cr^{6+} [29]. For Cr^{3+} octahedral coordination with a crystal field value of 10Dq=1.2 eV, and a charge transfer energy value Δ=7 gave the best accordance with the experimental spectra. The other parameters used for this simulation were (F_{dd}, F_{pd}, G_{pd})=0.9, SO=1.04, U_{pd}-U_{dd} =1 eV, e_g =1.35 eV and t_{2g}=0.65 eV. For Cr^{6+} tetrahedral coordination with a crystal field value of 10Dq=1.1 eV, and a charge transfer energy value Δ=2 eV were used. The other parameters used for this simulation were (F_{dd}, F_{pd}, G_{pd})=0.7, SO=1.05, Dt=0.1 eV, Ds=-0.1 eV, e_g =5 eV and t_{2g}=0 eV.

3. Results and Discussion

3.1. Thermal stability of LSCrF surface under O_2 and H_2O environments

Initially, the chemical stability of the LSCrF electrode in equilibrium with 0.5 mbar O_2 or H_2O atmospheres at 3 characteristic temperatures 450, 740 and 890 °C was evaluated. The measurements were performed as follows: first, the sample was annealed at the indicated temperature and atmospheric conditions for 10 min and subsequently the temperature was decreased to 350 °C in the same gas atmosphere for NAP-XPS and NEXAFS measurements. Each gas atmosphere experiment (O_2 or H_2O) was performed on a fresh sample in order to avoid the influence of possible aging phenomena on the starting material.

3.1.1. Surface oxidation state

Photoemission spectra of the Sr 3d and Cr 2p regions measured after annealing at 450 and 890 °C in O_2 or H_2O atmospheres are displayed in figures 1a and b. The Sr 3d peak (figure 1a) is composed of two doublets at 131.5±0.1 eV and 133.1±0.1 eV which according to depth profiling measurements (Figure S2a) are assigned to subsurface (subs-SrO) and surface (s-SrO) Sr species respectively, in agreement with previous reports on Sr-containing perovskites [30]. The subs-SrO Sr 3d component is enhanced in H_2O as compared to O_2, while for both atmospheres it decreases with the annealing temperature due to surface enrichment with s-SrO species.

The Cr 2p spectra measured in H_2O have a characteristic binding energy (576.2±0.1 eV) and peak shape previously attributed to chromium in the Cr^{3+} oxidation state [30,31] and it is unaffected by the

annealing temperature (Figure 1b). By contrast, in O_2 a new feature appears at the higher binding energy side and its intensity is enhanced with temperature. Deconvolution of the Cr 2p is complicated by the asymmetry at the high BE side of the peak which is a characteristic of chromium oxides, with the exception of Cr^{6+} valence. Therefore the Cr 2p peak profile recorded in H_2O was used to fit the low BE feature and an extra symmetric peak was added for the high BEs component. The fitting procedure provided two Cr 2p components at 576.2 eV and 580 ±0.1 eV ascribed to Cr^{3+} and Cr^{6+} species, respectively [31]. Depth profiling measurements (Figure S2b) show that the peak at 580 eV attributed to Cr^{6+} diminishes when increasing analysis depth, suggesting that Cr^{6+} is segregated over the Cr^{3+} cations located in the bulk of the perovskite phase.

The Cr $L_{3,2}$ edge of NEXAFS spectra are sensitive to the oxidation state and the local symmetry of chromium oxides and provide not only an important confirmation of photoemission results but also some additional insights. Figure 1c shows the Cr L_3 edge measured after annealing at 890 °C in H_2O and O_2, while the calculated difference between the two spectra peaks is included at the bottom of the figure. The Cr $L_{3,2}$ edge spectra recorded at lower temperatures can be found in figure S3. In addition, theoretically simulated spectra for tetrahedrally (O_{Td}) and octahedrally coordincated (O_h) Cr^{6+} and Cr^{3+} species respectively, have been included in the graph for comparison. The Cr L_3 edge measured in H_2O resembles the theoretical Cr^{3+} (O_h) peak and is in good agreement with previously reported spectra of Cr_2O_3 [32,33]. This confirms the presence of Cr^{3+} species, while the fact that it is not dependent on the annealing temperature (figure S3a) validates the stability of Cr^{3+} in H_2O already shown by NAP-XPS. The difference curve matches the theoretical Cr^{6+} (O_{Td}) while also resembles previously reported spectra of hexavalent chromium compounds such as K_2CrO_4 [32], $PbCrO_4$ [34] and $SrCrO_4$ [35] but deviates from that of CrO_3 powder [36]. NEXAFS spectra validate the photoemission results in O_2 showing partial oxidization of Cr^{3+} cations to Cr^{6+} and indicates possible reaction of Cr^{6+} cations with SrO to form $SrCrO_4$ compound. This is in accordance with earlier findings showing that surface segregated Sr from the A-site of the perovskite lattice is prone to react with volatile Cr species [37]. It is worth noting that in our previous work on LSCrF electrodes we found an evident increase of Sr surface concentration, but unlike in the present case formation of Cr^{6+} was not observed [30]. This difference should be mainly attributed to the significantly higher annealing temperatures employed in this work (up to 890 °C) as compared to [30] (up to 500 °C) in agreement with previous findings [38].

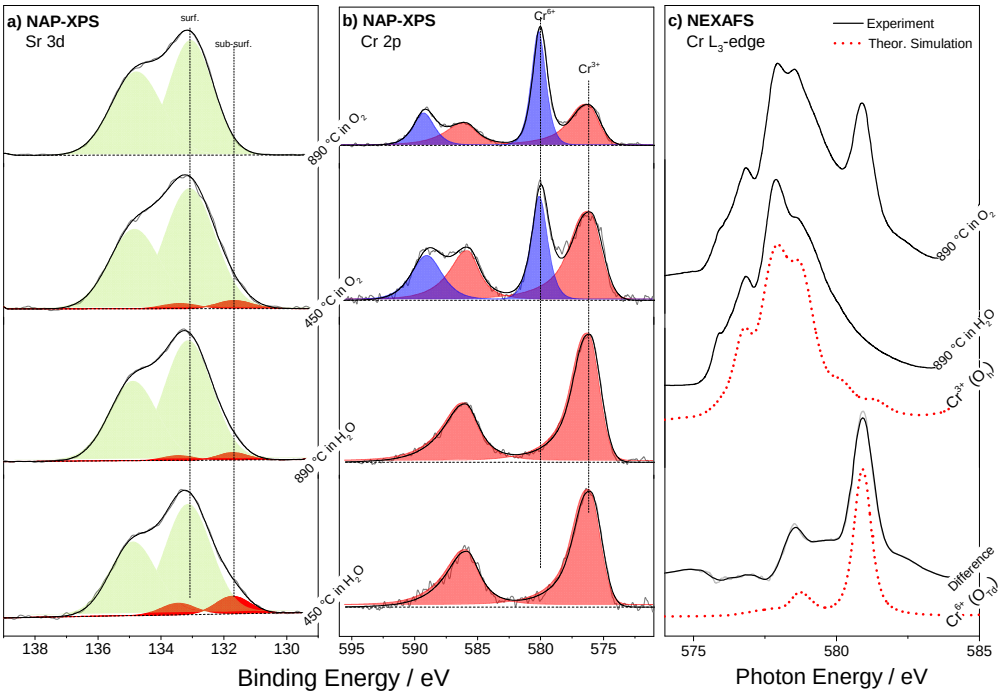

Figure 1. NAP-XPS (a) Sr 3d (hv = 325 eV), (b) Cr 2p (hv = 770 eV) spectra recorded on a LSCrF electrode after annealing for 10 min at the conditions indicated in the figure. For clarity, the spectra are normalized to the background and offset (c) Cr L_3-edge TEY-NEXAFS spectra (top) recorded on an LSCrF electrode after annealing for 10 min at the conditions indicated in the figure. The lower curve (diff.) is obtained after subtracting the spectrum recorded in H_2O from that in O_2 after proper normalization. Theoretically simulated Cr L_3-edge spectra (dot lines) for octahedrally coordinated Cr^{3+} (O_h) and tetrahedrally coordinated Cr^{6+} (O_{Td}) cations are included for comparison.All spectra are intensity normalized.

The formation of $SrCrO_4$ is also indicated by the XRD analysis of the electrode after the oxidation treatment. X-ray diffraction (XRD) patterns of O_2 treated-LSCrF are shown in Figure S4. The XRD analysis showed the expected phases of LSCrF according to the JCPDS data of PDF #70-2695, and the strong diffraction peaks of YSZ (JCPDS 70-4436) electrolyte support as indexed in Figure S4. In addition, four new peaks were observed between 24° and 30°, which can be assigned to the characteristic peaks of $SrCrO_4$ (JCPDS file No 35-0743).

The La $3d_{5/2}$ spectra, shown in figure S5a, consists of two main photoelectron lines at 834.6 and 851.3 eV and their corresponding shake-up satellite peaks located at about 4 eV higher in binding energy. The La 3d spectra are not considerably affected by the treatment conditions while corresponding to La^{3+} cations [30,39]. The Fe $2p_{3/2}$ spectrum (Figure S5b) is centred at about 711 eV as expected for Fe^{3+} cations [40], however due to the low signal-to-noise ratio, it is difficult to perform a detailed analysis of the iron valence during the various treatments and hence the chemical state of iron cations will not be discussed in detail here.

3.1.2 Surface composition

The intensity of core-level photoemission spectra can provide information about relative changes in the surface composition during the various treatments. Figure 2a compares the evolution of the cationic surface concentration in H_2O and O_2 as a function of the annealing temperature. In both environments, La and Fe decrease while Cr and Sr increase, with annealing temperature. The variations are notably higher in O_2 as compared to H_2O atmosphere. In particular, annealing in O_2 at 890 °C increases the Cr (B-site) concentration by a factor of two and reduces this of La (A-site) almost to the half as compared to 450°C. This result indicates that annealing at high temperature influences the cation distribution causing surface segregation of Cr and Sr cations over La and Fe. Please note that the surface composition deviates from the nominal bulk stoichiometry at almost all annealing temperatures and atmospheres. This might be due to inaccuracies either of the theoretical sensitivity factors or to the cation distribution model (homogenous) used for the calculations. Therefore only the relative changes of composition and not its absolute values will be discussed here.

In order to distinguish the arrangement between Cr and Sr, we present in figure 2b the Cr 3d and Sr 3d peak area ratio (Cr/Sr), which is characteristic of the relevant amount of the two cations at the outermost surface layers. In H_2O, the Cr/Sr ratio decreases with temperature reflecting a progressive segregation of Sr over Cr cations located in the perovskite lattice. On the contrary, in O_2 atmosphere the Cr/Sr ratio increases with temperature, which implies that in this case surface Sr is gradually replaced by Cr cations. Overall, the results presented above demonstrate that in O_2 the Cr^{3+} cations are partially oxidized to Cr^{6+} and diffuse over the outermost surface layers of the electrode. Analysis of the NEXAFS spectra indicated that Cr^{6+} species are most probably react with s-SrO to form $SrCrO_4$ in agreement with several previous findings regarding Cr deposition over SrO containing surfaces [41,42]. Oxidation of Cr was not observed when the electrode is treated in H_2O atmosphere and, in this case, it is mainly Sr segregation that dominates the surface. A schematic representation of the proposed surface composition in each atmosphere is given in figure 2c. Cr surface enrichment in O_2 is remarkable taking into account the fact that B-site cations of perovskite oxides are considered to segregate to the surface in reducing and not oxidizing atmospheres [12]. Oxidation of Sr ions in the A site of the perovskite structure is well-known, but here we show that in oxidative atmospheres the B site (Cr) cation can be also oxidized and segregate to the surface. This knowledge will be used in the next paragraph in order to differentiate the effect of the applied current under reaction conditions from that of the reacting gas phase environment.

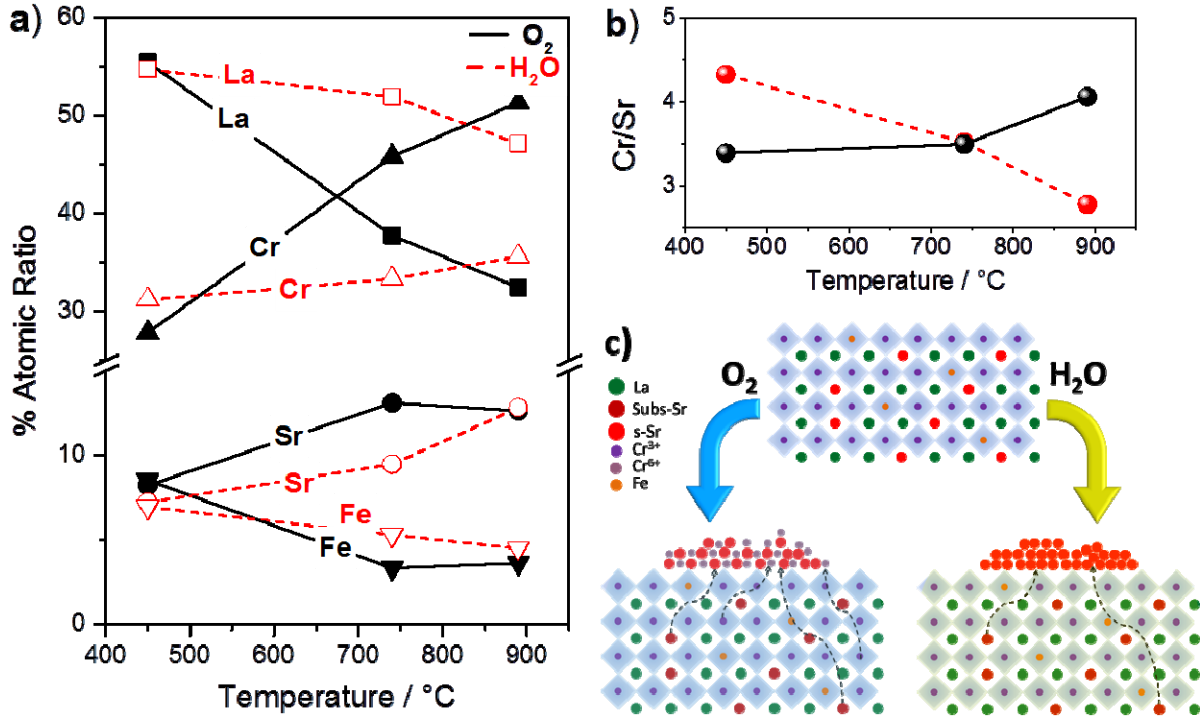

Figure 2. a) The cationic surface composition as a function of the annealing temperature in O_2 and H_2O atmospheres. The surface composition is calculated on the basis of the NAP-XPS peak areas measured for photoelectron peaks with 190 eV kinetic energy (estimated analysis depth 2 nm) and normalized by the theoretical sensitivity factors **b)** Ratio of Cr 2p/Sr 3d NAP-XPS core level intensities (recorded with photon energies of 770 and 325 eV respectively) recorded at conditions mentions above **c)** Schematic illustration of the proposed Sr and Cr surface arrangement upon high temperature annealing in H_2O and O_2 atmospheres.

3.1.3 Surface morphology

The morphology of the pristine and O_2 treated LSCrF electrodes was investigated by SEM and EDXS. Comparison of the surface morphology between pristine and O_2 treated LSCrF electrode (Figure S6) did not show any noticeable modifications, therefore in figure 3 typical SEM micrographs recorded on O_2 treated LSCrF are discussed. The SEM micrographs recorded in two different magnifications (figures 3a and c) demonstrate that the electrode is porous but the grain size is not uniform. It is composed of small particles with sizes between 0.1-0.2 microns, while few bigger particles of about 1-3 microns (indicated by an arrow in figure 3a and b) are noticed. The EDXS analysis (figure 3b) reveals that the bigger particles are rich in Sr, while Cr and La are homogeneously distributed all over the sample. In a higher magnification SEM image (figure 3d) it is seen that the surface of the particles is not smooth but exhibit clear facets and is decorated with small particles with a triangular shape. Formation of nanoparticles on the surface of bigger perovskite particles may involve cation segregation to the surface (often called exsolution), which is frequently observed in perovskite electrodes under high-temperature pretreatment and operation conditions [12].

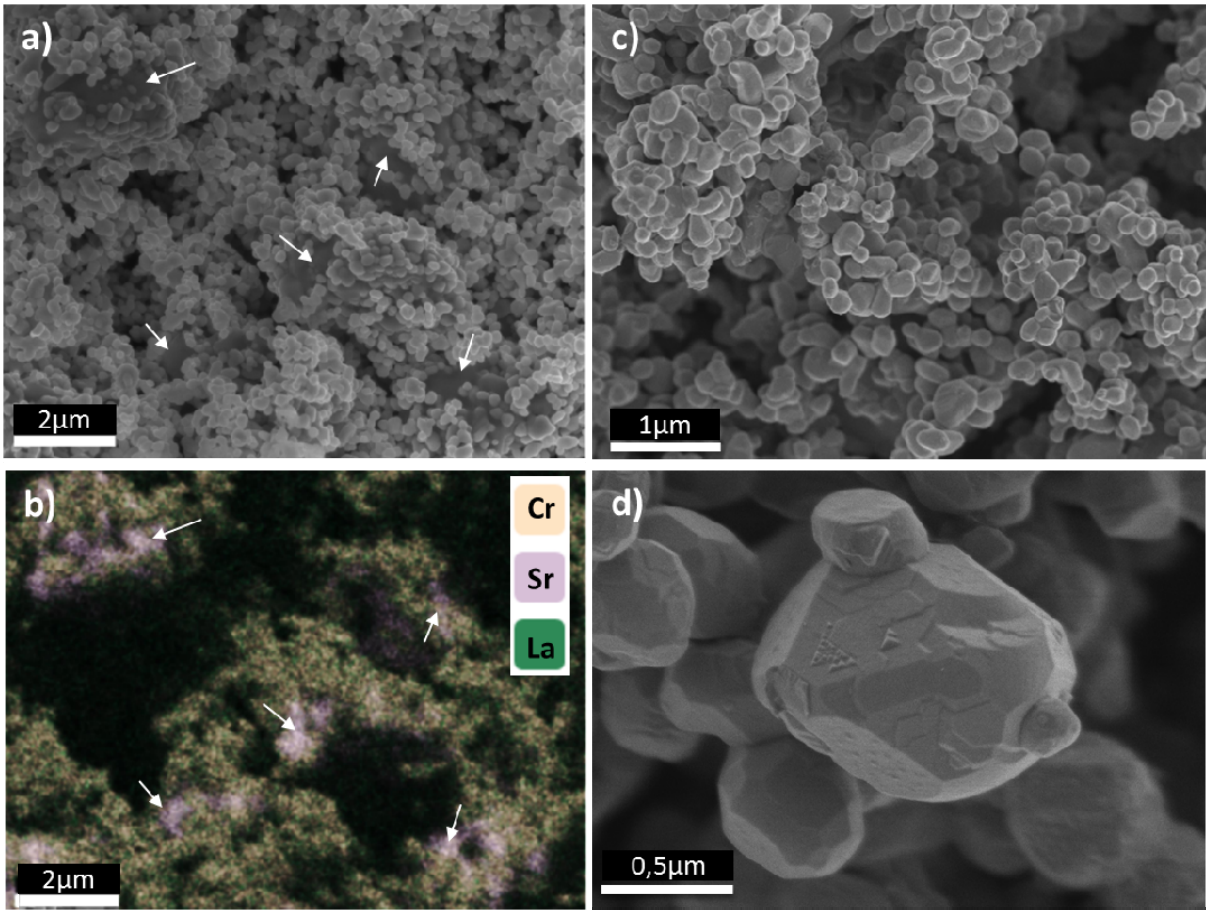

Figure 3. Characteristic top-view SEM micrographs, in various magnification levels, of the LSCrF electrode recorded after annealing for 30 min at 700 °C in air. Bigger particles are indicated with an arrow in fig. a. Fig. b shows the EDXS map of the image a, where Cr, Sr and La concentration is indicated by different colours (the EDXS signal of Fe was in the noise level, therefore it is not represented). Magnification a and b:x4500, c: x10000, d: 50000 times.

3.2 Evolution of the surface composition on LSCrF electrode during steam electrolysis

3.2.1 Electrode polarization in 100% H_2O environment

Having established the influence of the humid and oxidative environments on the surface oxidation state, in this part we use NAP-XPS to investigate LSCrF cathodes during steam electrolysis operation. Since, NAP-XPS analyses electrode areas away from the YSZ electrolyte and close to the current collector, it is essential to discuss first the implication of this zone to the electrochemical reaction. It is generally accepted that the area at the electrode/electrolyte interface is the most active region of the electrode during the electrochemical reaction.[43] However, what is crucial for the relevance of NAP-XPS measurements is the thickness of the electrochemical active region, sometimes also called the "Electrochemically Active Thickness, EAT". The EAT depends both on the microstructure and the operating conditions,[44] therefore reported values range from few to several tenths of microns. For example in case of Ni-YSZ electrodes EAT was calculated around 4 microns from the interface with YSZ electrolyte[45] while other reports extent this up to 30 micorns.[44] On GDC-based electrodes

the active region may extents inside to the whole volume of the electrode[46] while on perovskite LSM 22-31 % of overall electrochemical reaction occurs at the electrode/electrolyte interface and the rest inside the electrode above it.[47]

It has been previously shown that the overpotential can be directly measured by XPS without the need of a reference electrode.[48][49–51] B.W. Eichhorn and co-workers used this approach to determine the electrochemically active region of ceria-based model electrodes in water electrolysis and found that may extent up to 150 μm from the current collector.[49] In the present work the potential difference between the working (LSCrF) and counter (Pt) electrodes can be followed by measuring the BE shifts of the NAP-XPS spectra at different current densities. A linear correlation between the V_{W-C}, which reflects the potential losses inside the cell, and the shift of the valence band cut-off measured by NAP-XPS, is found as shown in figure S7. This validates the use of NAP-XPS since it demonstrates that the LSCrF zone close to the current collector is polarized by current flow and therefore it is actively involved in the electrochemical reaction.

The cell was subjected to galvanostatic steam electrolysis conditions by stepwise increasing the applied current while recording NAP-XPS spectra. Experiments were performed at a constant temperature of 700 °C and 1 mbar H_2O. Figure 4 shows the I-V characteristics obtained from an electrolyte-supported LSCrF/YSZ/Pt cell and the evolution of working electrode cationic composition based on *operando* NAP-XPS spectra. The potential between the LSCrF and Pt electrodes (V_{W-C}) is correlated with the overpotential on the cathode (LSCrF) via the measured BE shifts of the valence band given in the right-hand axis of figure 4 (for the correlation of BE shift and the potential please see figure S7) [49,52,53]. As expected, the V_{W-C}, and consequently the cell overpotential, is increasing with the applied current. The evolution of the surface takes place into two stages. First, up to 4 mA cm^{-2} the Sr concentration increases, while the concentration of the other cations decreases or remains stable, indicating segregation of Sr on the electrode surface. Notably, when currents higher than 4 mA cm^{-2} are applied the concentration of Sr stabilizes, or even slightly decreases, followed by a clear increase of Cr. La concentration decreases monotonically independently from the applied current, while Fe concentration is practically unaffected. The Cr/Sr intensity ratio shown at the top of Figure 4 firmly confirms that the surface arrangement between Cr and Sr is inverted with the application of current densities higher than 4 mA cm^{-2}.

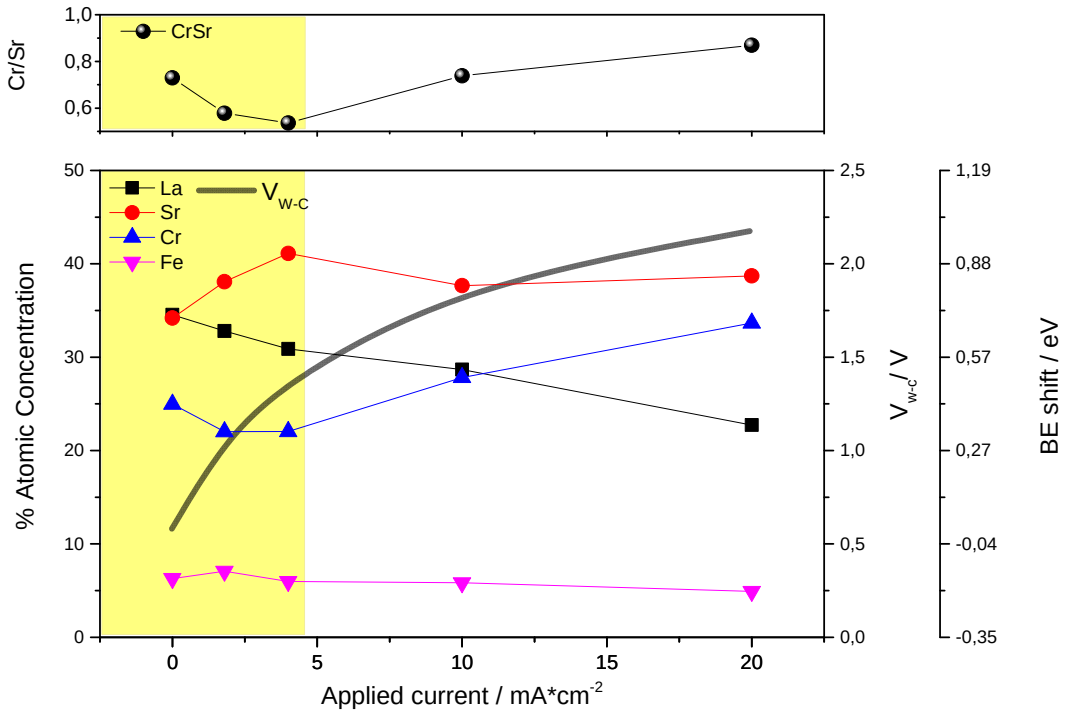

Figure 4. The surface cationic concentration (solid points) and the evolution of the potential measured between the LSCrF and the Pt electrodes (V_{W-C}) as a function of the applied current at 700 °C and 1 mbar H_2O. The corresponding binding energy shift of the valence band measured with NAP-XPS for each V_{W-C} is shown at the right-side axis. The top graph shows the Cr 2p/Sr 3d NAP-XPS intensity ratio. The part of the graph highlighted in yellow corresponds to the operation conditions associated to the segregation of Sr on the electrode surface. (Estimated analysis depth:1.3 nm)

The evolution of the LSCrF electrode surface composition with the applied current can be interpreted considering the modification of the Cr oxidation state during polarization. As is evident by the Cr 2p peak shown in figure 5, up to 4 mA cm^{-2} Cr remains in the Cr^{3+} state while above this current the characteristic contribution of Cr^{6+} appears in the Cr 2p spectrum. Therefore, similar to the observations in O_2 atmosphere (figure 2), oxidation of Cr^{3+} to Cr^{6+} is accompanied by surface enrichment of Cr, implying that segregation of Cr is driven by the changes in its oxidation state.

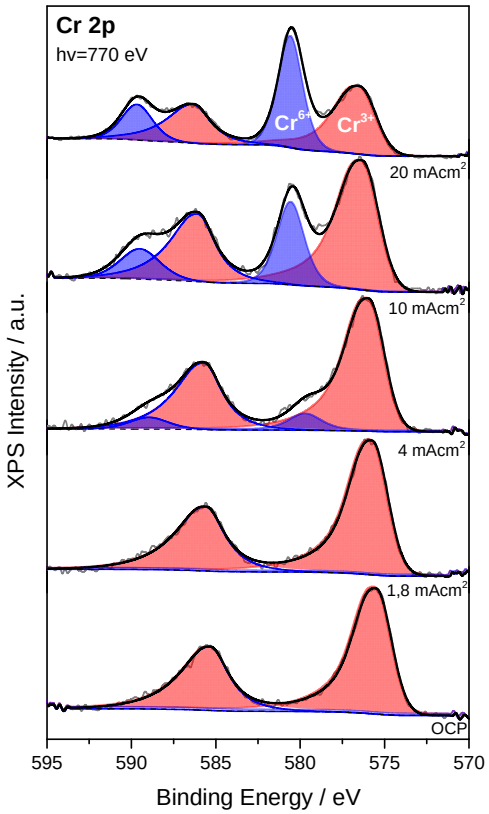

Figure 5. NAP-XPS Cr 2p spectra (hv = 770 eV) recorded on an LSCrF electrode at different current densities (indicated in the figure) under 1 mbar H_2O at 700 °C. The spectra are normalized to the background and offset for clarity.

The Sr 3d spectra are dominated by the surface component (Figure S8) around 133 eV, while apart from an evident shift of the peak due to the induced overpotential, the peak shape is not modified. Since, as shown in Figure 1, further oxidization of Cr^{3+} cations is not happening in H_2O atmosphere, its observation during H_2O electrolysis experiments should be related to the increased oxygen partial pressure on the electrode. This can be caused either electrochemically by the applied current or thermochemically due to O_2 produced at the anode side. In the first scenario one can argue that after water dissociation, O^{2-} anions are formed and while migrating towards the counter electrode react with Cr^{3+} to form Cr^{6+}. Obviously, these oxygen anions will not reach the anode electrode, therefore, the measured electrochemical current will be lower. According to the second scheme, in the NAP-XPS setup both electrode sides faces the same gas environment (single chamber cell), therefore unavoidable the cathode will exposed to gas phase O_2 produced in the anode side during steam electrolysis. To clarify this point we have used ex situ XPS to measure LSCrF electrodes from conventional two compartments LSCrF/YSZ/LSM cells after polarization in steam electrolysis conditions. The Cr 2p spectra (not shown here) indicated the presence of the Cr^{6+} component at the cathode LSCrF electrode after operation, which was not the case of pristine LSCrF. This result suggest

that the origin of the Cr^{6+} species in the NAP-XPS measurements is related to the measured potential (at least in part) and is not solely the consequence of molecular oxygen produced at the anode side of the cell. In either case, surface oxidation of the LSCrF electrode during steam electrolysis will be exploited in the next sections in order to deliver valuable information about the electrode deactivation paths.

3.2.2 Electrode polarization in H_2/H_2O mixture

The Cr^{6+} component in the Cr 2p spectrum, which is characteristic of surface $SrCrO_4$ formation, progressively disappears upon annealing the electrode at 700 °C in H_2/H_2O mixture for about 1 hour. This is in accordance with previous temperature-programmed reduction studies in H_2 of bulk $SrCrO_4$ compounds which showed that reduction takes place in the temperature range between 500 and 700 °C [54]. After reduction, the surface is dominated by s-SrO and Cr^{3+} cations in accordance with the expected products of $SrCrO_4$ reduction [54]. Consequently, electrolysis experiments were performed in H_2/H_2O mixture. The i-V curve in H_2/H_2O shown in figure 6, is similar to the one measured in H_2O, but with slightly higher $V_{W\text{-}C}$ voltages and significantly higher overpotentials. The perovskite composition presented in the same graph shows that the surface is dominated by s-SrO, which is increasing even further with the applied current. The concentration of Cr^{3+}, which was quite significant at the initial state, withdraw progressively as can be observed in the Cr/Sr peak area ratio shown at the top of the figure 6. The analysis of Cr 2p photoemission spectra show that the addition of H_2 in H_2O feed prevents oxidation of Cr^{3+} to Cr^{6+} at all the applied currents (see figure S9) and evidently suppress the driving force for Cr surface segregation. This experiment affirms that surface segregation of Cr is directly related to its oxidation state and is only observed when Cr^{3+} is oxidized to Cr^{6+} either thermochemically or electrochemically.

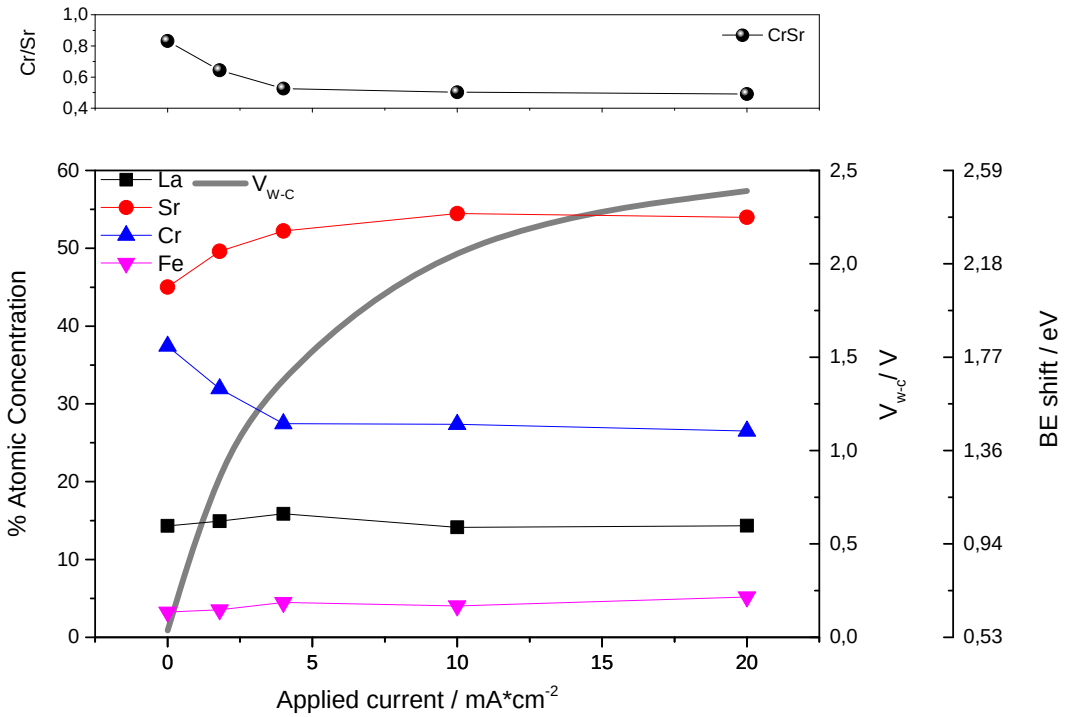

Figure 6. The surface cationic concentration (solid points) and the evolution of the potential measured between the LSCrF and the Pt electrodes (V_{W-C}) as a function of the applied current at 700 °C and 1 mbar H_2O/H_2 (1/1). The top graph shows the Cr 2p / Sr 3d NAP-XPS intensity ratio.

3.3 Effect of the surface state on the LSCrF electrode performance during steam electrolysis

In order to examine the effect of surface $SrCrO_4$ formation on the electrochemical performance, we compare the cell overpotential under upward and downward polarization where the cathode electrode surface contains different amounts of Cr^{6+} species. Figure 7a presents the i-V (the overpotential was measured by the valence band maximum shift) curves of a cell measured under electrolysis conditions during the upward (increasing current) and downward (decreasing current) galvanostatic cycles (the current was applied for about 45 min in each step). As expected, the overpotential increases monotonically with the applied current, however, for the same current densities lower overpotentials were required at the downward cycle as compared to those of the upward. Practically, this implies that the cell electrolysis performance has been improved during the downward polarization cycle.

Operando NAP-XPS results can help to elucidate the improvement of the LSCrF cathode performance. Since the segregation of Cr^{6+} and Sr cations to the surface under these conditions were clearly shown above, we focus on the detailed understanding of their role in the reactivity. Figure 7b presents the ratio between $SrCrO_4$ and SrO deduced by the analysis of Cr 2p and Sr 3d NAP-XPS spectra (for more details on the calculation of this ratio please refer to supporting information 10).

The $SrCrO_4$/SrO ratio can give a direct measure of the relative amount of the two compounds on the LSCrF surface, helping to compare their influence on the electrode performance. Initially, the electrode surface is dominated by segregated surface SrO (estimated average thickness around 1-2 nm) which is expected to negatively influence the electrochemical performance [55]. As seen in figure 7b, during the upward electrolysis cycle the $SrCrO_4$/SrO increases monotonically suggesting that $SrCrO_4$ is gradually formed at the expense of the initially present SrO. However, after the maximum applied current (20 mA cm^2) and during the consequent downward electrolysis cycle, the ratio remains practically stable at around 0.8. Keeping in mind that the expected surface stoichiometry of Sr and Cr in $SrCrO_4$ is 1, this ratio implies that the great majority of the initially present s-SrO has been transformed to $SrCrO_4$. Accordingly, it becomes clear that the improvement of the cell performance shown in figure 7a is correlated with the partial replacement of SrO_x by $SrCrO_x$ on the perovskite cathode surface.

Electrochemical impedance spectroscopy (EIS) is often used in order to distinguish the contribution of different cell components or processes to the total electrode impedance. The galvanostatic EIS spectra measured at 10 mA cm^{-2} during the up and down potential cycles are compared in the Nyquist plots given in the inset of figure 7a. Commonly, in the Nyquist plot the high-frequency intercept of the real axis represents the ohmic resistance (R_{Ohm}), while the difference between the high frequency and low-frequency intercepts corresponds to the electrode polarization resistance (R_p). The R_{Ohm} includes both electronic and ionic resistances, while R_p reflects the reaction kinetics typically influenced by electrochemical, gas diffusion and conversion resistances. It can be seen that the R_{Ohm} decreases about 12 Ohm cm^2 in the downward cycle. This suggests an increase of the electronic and ionic conductance of the electrochemical cell in the downward cycle. Since the temperature is constant the ionic conductance of YSZ should be considered stable and the R_{Ohm} decrease mainly attributed to changes in the electrode conductivity. In addition, the decrease of R_{Ohm} is accompanied by a decrease of R_p of about 7 Ohm cm^2, which can be assigned to the improvement of the reaction kinetics in the downward cycle. Since NAP-XPS results showed that SrO has been replaced by $SrCrO_4$ at the surface of the LSCrF electrode during the downward cycle, it is reasonable to assume that the $SrCrO_4$ improves the electrical conduction and the electrocatalytic activity of the LSCrF electrode, as compared to its previous state where the surface was dominated by SrO.

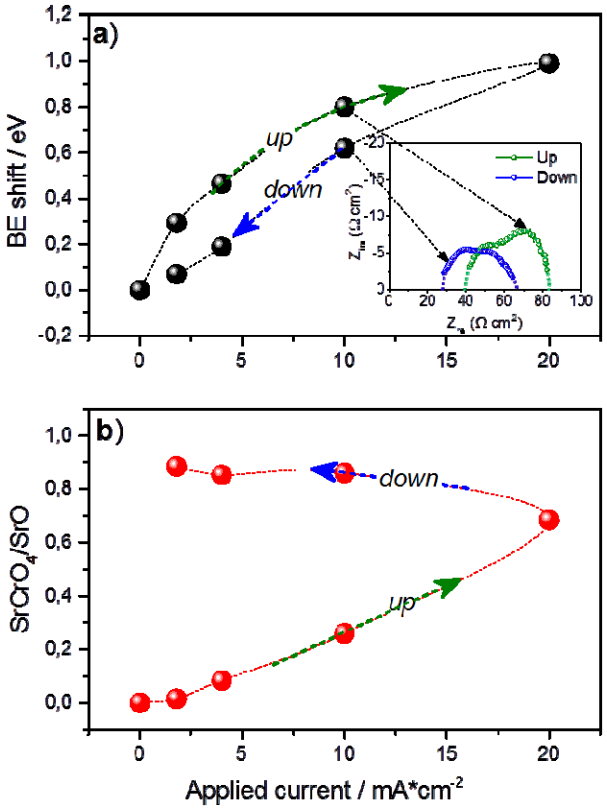

Figure 7. a) The shift of the Fermi edge as compared to O.C.P conditions (derived by NAP-XPS spectra recorded using 725 eV photon energy and corresponding to the overpotential) of an electrochemical cell with LSCrF cathode electrode as a function of the applied current density. Measurements were performed at 700 °C and at constant H_2O pressure of 1 mbar during consecutive current step-up and -down cycles. The inset shows impedance spectra presented in Nyquist form, obtained under constant applied current of -10 mA cm^{-2}. b) The ratio between $SrCrO_x/SrO_x$ derived by the analysis of Cr 2p and Sr 3d NAP-XPS peaks at the conditions mentioned in a.

Sr enrichment in the surface region is well documented in perovskites containing Sr at the A-cation site and is often associated with the decrease of the electrocatalytic activity of the oxygen electrodes under fuel cell operation conditions [55,56]. Recent studies on perovskite oxygen electrodes proposed that Sr segregation may be prevented under polarization, leading to more stable and efficient electrochemical cells [57]. Apart from Sr segregation, another common cause of cell performance degradation is chromium deposition on the electrode coming from the stainless steel components of the cell [58]. It has been reported that surface Sr oxides readily reacts with volatile Cr species to form $SrCrO_4$ [35,59] according to the reaction $2SrO+Cr_2O_3+3/2O_2 \rightarrow 2SrCrO_4$ [60]. Here, we found that the appearance of $SrCrO_4$ on the surface of the LSCrF electrode does not poison the cell, but on the contrary enhances its performance as compared to its prior state. Before trying to elucidate this effect, it is necessary to establish the fundamental difference between the mechanisms of Cr deposition on electrodes containing Cr in their lattice, like the LSCrF perovskite and studies

where the chromium source is external to the electrode, e.g. the stainless steel interconnect components.

First of all, previous studies looking at the effect of surface chromites were dealing with significantly higher Cr deposition amounts (e.g. able to reproduce clear diffraction patterns in the XRD diagrams) [60,61] coming from volatile chromium oxide compounds. Deposited Cr is thought to block the electrochemically active sites and/or the decrease of the electrode conductivity [38]. The present work has two basic differences as compared to the previous Cr deactivation studies. First $SrCrO_4$ exists in very low quantities as compared to the electrode volume, with an average thickness which should not exceed the analysis depth of NAP-XPS method, even if some thicker areas able to produce the XRD diffraction pattern of $SrCrO_4$ are not excluded. This implies that, in contrast with typical Cr poisoning effect [60], $SrCrO_4$ formation does not induce changes in the electrode porosity (as also shown by SEM) which can hinder the gas transport into the cathode. Second, $SrCrO_4$ is not an additional compound deposited on the surface from the gas phase but is induced by bulk Cr cation diffusion. Notably when Cr is segregated onto the surface of the electrode reacts with Sr and replaces the previously existing SrO surface layer. Therefore $SrCrO_4$ formation should be considered as a way to mitigate the detrimental effect of SrO surface layer [62]. This is consistent with the significantly lower intrinsic band gap of $SrCrO_4$ (2.45 eV) [63] as compared to SrO (ca. 6 eV) [64] which is expected to enhance the LSCrF cathode conductance. In addition, the formation of oxygen vacancies is promoted on chromate compounds [65], which in turn might improve the electrochemical reaction kinetics. Our electrocatalytic results show that the addition of segregated Cr on the surface of the perovskite cathode contributed to the overall stability of SOEC cell, since it reduces the negative effects caused by the unavoidable Sr cation segregation. Therefore, at least in this particular case, surface Cr should be consider as a promoter, instead of being a poison, of the SOEC cell performance.

Conclusions

We have shown here that besides the well-known Sr segregation on the surface of perovskite electrodes, the B-site Cr cation can also segregate in oxidative conditions. This segregation is driven by oxidation of Cr^{3+} cations to Cr^{6+} and can take place upon steam electrolysis without the presence of H_2. In contrast with the expected deactivation effect of chromium previously described for solid oxide cell electrodes, our operando studies suggest that Cr^{6+} does not inhibit, but rather promotes the electrode performance during electrolysis. A possible scenario which can explain the positive role of Cr^{6+} is the suppression of surface SrO which is known to be detrimental for the performance of perovskite electrodes.

Acknowledgments

The research leading to these results has received funding from the Fuel Cells and Hydrogen 2 Joint Undertaking under the project SElySOs with grant agreement No 671481. This Joint Undertaking receives support from the European Union's Horizon 2020 research and innovation programme and Greece, Germany, Czech Republic, France, Norway. Beamtime expenses has been partly supported by the project CALIPSOplus under the Grant Agreement 730872 from the EU Framework Programme for Research and Innovation HORIZON 2020. L.P.Z. and D.K.C. would like to thank the China Scholarship Council (CSC) for supporting their studies at ICPEES. We thank Prof. R. Schlögl and Dr. D. Niakolas for their useful and constructive comments. Finally, we acknowledge HZB for the allocation of synchrotron radiation beamtime and ALBA Synchrotron staff for the collaboration during the experiments. '

References

[1] M.A. Laguna-Bercero, Recent advances in high temperature electrolysis using solid oxide fuel cells: A review, J. Power Sources. 203 (2012) 4–16. doi:10.1016/j.jpowsour.2011.12.019.

[2] C. Sun, R. Hui, J. Roller, Cathode materials for solid oxide fuel cells: a review, J. Solid State Electrochem. 14 (2010) 1125–1144. doi:10.1007/s10008-009-0932-0.

[3] J. Schefold, A. Brisse, H. Poepke, Long-term Steam Electrolysis with Electrolyte-Supported Solid Oxide Cells, Electrochim. Acta. 179 (2015) 161–168. doi:10.1016/j.electacta.2015.04.141.

[4] J. Schefold, A. Brisse, H. Poepke, 23,000 h steam electrolysis with an electrolyte supported solid oxide cell, Int. J. Hydrogen Energy. 42 (2017) 13415–13426. doi:10.1016/j.ijhydene.2017.01.072.

[5] S.Y. Gómez, D. Hotza, Current developments in reversible solid oxide fuel cells, Renew. Sustain. Energy Rev. 61 (2016) 155–174. doi:10.1016/J.RSER.2016.03.005.

[6] B. Hua, M. Li, Y.-F. Sun, J.-H. Li, J.-L. Luo, Enhancing Perovskite Electrocatalysis of Solid Oxide Cells Through Controlled Exsolution of Nanoparticles, ChemSusChem. 10 (2017) 3333–3341. doi:10.1002/cssc.201700936.

[7] S. Tao, J.T.S. Irvine, A redox-stable efficient anode for solid-oxide fuel cells., Nat. Mater. 2 (2003) 320–323. doi:10.1038/nmat871.

[8] X. Yang, J.T.S. Irvine, (La0.75Sr0.25)0.95Mn0.5Cr0.5O3 as the cathode of solid oxide electrolysis cells for high temperature hydrogen production from steam, J. Mater. Chem. 18 (2008) 2349–2354. doi:10.1039/b800163d.

[9] K.-M. Papazisi, D. Tsiplakides, S. Balomenou, High Temperature Co-Electrolysis of CO_2 and Water on Doped Lanthanum Chromites, ECS Trans. 78 (2017) 3197–3204. doi:10.1149/07801.3197ecst.

[10] S. Gunduz, D.J. Deka, U.S. Ozkan, Advances in High-Temperature Electrocatalytic Reduction of CO2 and H2O, in: 2018: pp. 113–165. doi:10.1016/bs.acat.2018.08.003.

[11] K.A. Stoerzinger, Y. Du, K. Ihm, K.H.L. Zhang, J. Cai, J.T. Diulus, R.T. Frederick, G.S. Herman, E.J. Crumlin, S.A. Chambers, Impact of Sr-Incorporation on Cr Oxidation and Water Dissociation in $La_{(1-x)}Sr_xCrO_3$, Adv. Mater. Interfaces. 5 (2018) 1701363. doi:10.1002/admi.201701363.

[12] Y. Li, W. Zhang, Y. Zheng, J. Chen, B. Yu, Y. Chen, M. Liu, Controlling cation segregation in perovskite-based electrodes for high electro-catalytic activity and durability, Chem. Soc. Rev. (2017). doi:10.1039/c7cs00120g.

[13] A.K. Opitz, A. Nenning, C. Rameshan, M. Kubicek, T. Götsch, R. Blume, M. Hävecker, A. Knop-Gericke, G. Rupprechter, B. Klötzer, J. Fleig, Surface Chemistry of Perovskite-Type Electrodes During High Temperature CO_2 Electrolysis Investigated by *Operando* Photoelectron Spectroscopy, ACS Appl. Mater. Interfaces. 9 (2017) 35847–35860. doi:10.1021/acsami.7b10673.

[14] J.H. Myung, D. Neagu, D.N. Miller, J.T. Irvine, Switching on electrocatalytic activity in solid oxide cells, Nature. 537 (2016) 528–531. doi:10.1038/nature19090.

[15] K.M. Papazisi, S. Balomenou, D. Tsiplakides, Synthesis and characterization of La0.75Sr0.25Cr0.9M0.1O3 perovskites as anodes for CO-fuelled solid oxide fuel cells, J. Appl. Electrochem. 40 (2010) 1875–1881. doi:10.1007/s10800-010-0150-6.

[16] F.M. Sapountzi, S. Brosda, K.M. Papazisi, S.P. Balomenou, D. Tsiplakides, Electrochemical performance of La <inf>0.75</inf>Sr <inf>0.25</inf>Cr <inf>0.9</inf>M <inf>0.1</inf>O <inf>3</inf> perovskites as SOFC anodes in CO/CO <inf>2</inf> mixtures, J. Appl. Electrochem. 42 (2012). doi:10.1007/s10800-012-0459-4.

[17] P. Kim-Lohsoontorn, Y.M. Kim, N. Laosiripojana, J. Bae, Gadolinium doped ceria-impregnated nickel-yttria stabilised zirconia cathode for solid oxide electrolysis cell, Int. J. Hydrogen Energy. 36 (2011) 9420–9427. doi:10.1016/j.ijhydene.2011.04.199.

[18] V. Pérez-Dieste, L. Aballe, S. Ferrer, J. Nicolàs, C. Escudero, A. Milán, E. Pellegrin, Near Ambient Pressure XPS at ALBA, J. Phys. Conf. Ser. 425 (2013) 072023. doi:10.1088/1742-6596/425/7/072023.

[19] A. Knop-Gericke, E. Kleimenov, M. Hävecker, R. Blume, D. Teschner, S. Zafeiratos, R. Schlögl, V.I. Bukhtiyarov, V. V. Kaichev, I.P. Prosvirin, A.I. Nizovskii, H. Bluhm, A. Barinov, P. Dudin, M. Kiskinova, Chapter 4 X-Ray Photoelectron Spectroscopy for Investigation of Heterogeneous Catalytic Processes, Adv. Catal. 52 (2009) 213–272. doi:10.1016/S0360-0564(08)00004-7.

[20] W.H. Doh, V. Papaefthimiou, S. Zafeiratos, Applications of Synchrotron-Based X-Ray Photoelectron Spectroscopy in the Characterization of Nanomaterials, 2015. doi:10.1007/978-3-662-44551-8_9.

[21] C.J. Powell, A. Jablonski, Progress in quantitative surface analysis by X-ray photoelectron spectroscopy: Current status and perspectives, J. Electron Spectros. Relat. Phenomena. 178–179 (2010) 331–346. doi:10.1016/j.elspec.2009.05.004.

[22] A. Jablonski, Evaluation of procedures for overlayer thickness determination from XPS intensities, Surf. Sci. (2019). doi:10.1016/j.susc.2019.05.004.

[23] J.J. Yeh, I. Lindau, Atomic subshell photoionization cross sections and asymmetry parameters: 1 <Z< 103, At. Data Nucl. Data Tables. 32 (1985) 1–155. doi:10.1016/0092-640X(85)90016-6.

[24] B.H. Frazer, B. Gilbert, B.R. Sonderegger, G. De Stasio, The probing depth of total electron yield in the sub-keV range: TEY-XAS and X-PEEM, Surf. Sci. 537 (2003) 161–167. doi:10.1016/S0039-6028(03)00613-7.

[25] F. De Groot, High-resolution X-ray emission and X-ray absorption spectroscopy, Chem. Rev. 101 (2001) 1779–1808. doi:10.1021/cr9900681.

[26] H. Ikeno, F.M.F. de Groot, E. Stavitski, I. Tanaka, Multiplet calculations of L 2,3 x-ray absorption near-edge structures for 3d transition-metal compounds, J. Phys. Condens. Matter. 21 (2009) 104208. doi:10.1088/0953-8984/21/10/104208.

[27] E. Stavitski, F.M.F. de Groot, The CTM4XAS program for EELS and XAS spectral shape analysis of transition metal L edges, Micron. 41 (2010) 687–694. doi:10.1016/j.micron.2010.06.005.

[28] A.S. Shkvarin, M. V. Yablonkikh, Y.M. Yarmoshenko, A.I. Merentsov, B. V. Senkovskiy, J. Avila, M. Asensio, A.N. Titov, Electronic structure of octahedrally coordinated Cr in CrxTiX2 (X = Se, Te) and TixCr1-xSe2, J. Electron Spectros. Relat. Phenomena. 206 (2016) 12–17. doi:10.1016/j.elspec.2015.11.001.

[29] M. Torres Deluigi, F.M.F. De Groot, G. L??pez-D??az, G. Tirao, G. Stutz, J. Riveros De La Vega, Core and valence structures in K?? X-ray emission spectra of chromium materials, J. Phys. Chem. C. 118 (2014) 22202–22210. doi:10.1021/jp409622r.

[30] F. Paloukis, K.M. Papazisi, T. Dintzer, V. Papaefthimiou, V.A. Saveleva, S.P. Balomenou, D. Tsiplakides, F. Bournel, J.J. Gallet, S. Zafeiratos, Insights into the Surface Reactivity of Cermet and Perovskite Electrodes in Oxidizing, Reducing, and Humid Environments, ACS Appl. Mater. Interfaces. 9 (2017) 25265–25277. doi:10.1021/acsami.7b05721.

[31] D. Chidambaram, G.P. Halada, C.R. Clayton, Development of a technique to prevent radiation damage of chromate conversion coatings during X-ray photoelectron spectroscopic analysis, Appl. Surf. Sci. 181 (2001) 283–295. doi:10.1016/S0169-4332(01)00433-0.

[32] C. Theil, J. van Elp, F. Folkmann, Ligand field parameters obtained from and chemical shifts observed at the Cr L2,3 edges, Phys. Rev. B. 59 (1999) 7931–7936. doi:10.1103/PhysRevB.59.7931.

[33] M. Asa, G. Vinai, J.L. Hart, C. Autieri, C. Rinaldi, P. Torelli, G. Panaccione, M.L. Taheri, S. Picozzi, M. Cantoni, Interdiffusion-driven synthesis of tetragonal chromium (III) oxide on BaTi O 3, Phys. Rev. Mater. 2 (2018) 033401. doi:10.1103/PhysRevMaterials.2.033401.

[34] T. Kendelewicz, P. Liu, C.S. Doyle, G.E. Brown, Spectroscopic study of the reaction of aqueous Cr(VI) with Fe3O4(111) surfaces, Surf. Sci. 469 (2000) 144–163. doi:10.1016/S0039-6028(00)00808-6.

[35] M. Finsterbusch, A. Lussier, J.A. Schaefer, Y.U. Idzerda, Electrochemically driven cation segregation in the mixed conductor La 0.6 Sr 0.4 Co 0.2 Fe 0.8 O 3 - δ, Solid State Ionics. 212 (2012) 77–80. doi:10.1016/j.ssi.2012.02.006.

[36] S.O. Kucheyev, B. Sadigh, T.F. Baumann, Y.M. Wang, T.E. Felter, T. van Buuren, A.E. Gash, J.H. Satcher, A. V. Hamza, Electronic structure of chromia aerogels from soft x-ray absorption spectroscopy, J. Appl. Phys. 101 (2007) 124315. doi:10.1063/1.2749489.

[37] L. Zhao, J. Drennan, C. Kong, S. Amarasinghe, S.P. Jiang, Insight into surface segregation and chromium deposition on La $_{0.6}$ Sr $_{0.4}$ Co $_{0.2}$ Fe $_{0.8}$ O $_{3-\delta}$ cathodes of solid oxide fuel cells, J. Mater. Chem. A. 2 (2014) 11114–11123. doi:10.1039/C4TA01426J.

[38] C.C. Wang, K. O'Donnell, L. Jian, S.P. Jiang, Co-Deposition and Poisoning of Chromium and Sulfur Contaminants on La $_{0.6}$ Sr $_{0.4}$ Co $_{0.2}$ Fe $_{0.8}$ O $_{3-\delta}$ Cathodes of Solid Oxide Fuel Cells, J. Electrochem. Soc. 162 (2015) F507–F512. doi:10.1149/2.0231506jes.

[39] M.F. Sunding, K. Hadidi, S. Diplas, O.M. Løvvik, T.E. Norby, A.E. Gunnæs, XPS characterisation of in situ treated lanthanum oxide and hydroxide using tailored charge referencing and peak fitting procedures, J. Electron Spectros. Relat. Phenomena. 184 (2011) 399–400. doi:10.1016/j.elspec.2011.04.002.

[40] V. Papaefthimiou, I. Florea, W. Baaziz, I. Janowska, W.H. Doh, D. Begin, R. Blume, A. Knop-Gericke, O. Ersen, C. Pham-Huu, S. Zafeiratos, Effect of the specific surface sites on the reducibility of ??-Fe 2O3/graphene composites by hydrogen, J. Phys. Chem. C. 117 (2013) 20313–20319. doi:10.1021/jp4067718.

[41] C.C. Wang, S. Darvish, K. Chen, B. Hou, Q. Zhang, Z. Tan, Y. Zhong, S.P. Jiang, Combined Cr and S poisoning of La0.8Sr0.2MnO3-δ (LSM) cathode of solid oxide fuel cells, Electrochim. Acta. 312 (2019) 202–212. doi:10.1016/j.electacta.2019.04.116.

[42] N. Ni, S.J. Cooper, R. Williams, N. Kemen, D.W. McComb, S.J. Skinner, Degradation of (La $_{0.6}$ Sr $_{0.4}$) $_{0.95}$ (Co $_{0.2}$ Fe $_{0.8}$)O $_{3-\delta}$ Solid Oxide Fuel Cell Cathodes at the Nanometer Scale and below, ACS Appl. Mater. Interfaces. 8 (2016) 17360–17370. doi:10.1021/acsami.6b05290.

[43] J.H. Nam, Electrochemically Active Thickness of Solid Oxide Fuel Cell Electrodes: Effectiveness Model Prediction, Bull. Korean Chem. Soc. 38 (2017) 477–483. doi:10.1002/bkcs.11116.

[44] K. Miyawaki, M. Kishimoto, H. Iwai, M. Saito, H. Yoshida, Comprehensive understanding of the active thickness in solid oxide fuel cell anodes using experimental, numerical and semi-analytical approach, J. Power Sources. 267 (2014) 503–514. doi:10.1016/j.jpowsour.2014.05.112.

[45] T. Nagasawa, K. Hanamura, Prediction of overpotential and effective thickness of Ni/YSZ anode for solid oxide fuel cell by improved species territory adsorption model, J. Power Sources. 353 (2017) 115–122. doi:10.1016/j.jpowsour.2017.03.154.

[46] M. Rahmanipour, A. Pappacena, M. Boaro, A. Donazzi, A Distributed Charge Transfer Model for IT-SOFCs Based on Ceria Electrolytes, J. Electrochem. Soc. 164 (2017) F1249–F1264. doi:10.1149/2.1911712jes.

[47] T. Nagasawa, K. Hanamura, Investigation of oxide ion flux at cathode/electrolyte interface in solid oxide fuel cell, J. Power Sources. 412 (2019) 695–700. doi:10.1016/j.jpowsour.2018.12.013.

[48] S. Ladas, S. Kennou, S. Bebelis, C.G. Vayenas, Origin of non-Faradaic electrochemical modification of catalytic activity, J. Phys. Chem. 97 (1993) 8845–8848. doi:10.1021/j100137a004.

[49] C. Zhang, M.E. Grass, A.H. McDaniel, S.C. DeCaluwe, F. El Gabaly, Z. Liu, K.F. McCarty, R.L. Farrow, M.A. Linne, Z. Hussain, G.S. Jackson, H. Bluhm, B.W. Eichhorn, Measuring fundamental properties in operating solid oxide electrochemical cells by using in situ X-ray photoelectron spectroscopy., Nat. Mater. 9 (2010) 944–9. doi:10.1038/nmat2851.

[50] C. Zhang, M.E. Grass, Y. Yu, K.J. Gaskell, S.C. DeCaluwe, R. Chang, G.S. Jackson, Z. Hussain, H. Bluhm, B.W. Eichhorn, Z. Liu, Multielement Activity Mapping and Potential Mapping in Solid Oxide Electrochemical Cells through the use of *operando* XPS, ACS Catal. 2 (2012) 2297–2304. doi:10.1021/cs3004243.

[51] V. Papaefthimiou, D.K.D.K. Niakolas, F. Paloukis, D. Teschner, A. Knop-Gericke, M. Haevecker, S. Zafeiratos, Operando observation of nickel/ceria electrode surfaces during intermediate temperature steam electrolysis, J. Catal. 352 (2017) 305–313. doi:10.1016/j.jcat.2017.06.005.

[52] Z.A. Feng, C. Balaji Gopal, X. Ye, Z. Guan, B. Jeong, E. Crumlin, W.C. Chueh, Origin of Overpotential-Dependent Surface Dipole at CeO2-x/Gas Interface during Electrochemical Oxygen Insertion Reactions, Chem. Mater. 28 (2016) 6233–6242. doi:10.1021/acs.chemmater.6b02427.

[53] L. Yu, Y. Takagi, T. Nakamura, O. Sekizawa, T. Sakata, T. Uruga, M. Tada, Y. Iwasawa, G. Samjeské, T. Yokoyama, Non-contact electric potential measurements of electrode components in an operating polymer electrolyte fuel cell by near ambient pressure XPS, Phys. Chem. Chem. Phys. 19 (2017) 30798–30803. doi:10.1039/C7CP05436J.

[54] R. Khobragade, H. Einaga, S. Jain, G. Saravanan, N. Labhsetwar, Sulfur dioxide-tolerant strontium

chromate for the catalytic oxidation of diesel particulate matter, Catal. Sci. Technol. 8 (2018) 1712–1721. doi:10.1039/C7CY02553J.
[55] G.M. Rupp, A.K. Opitz, A. Nenning, A. Limbeck, J. Fleig, Real-time impedance monitoring of oxygen reduction during surface modification of thin film cathodes, Nat. Mater. 16 (2017) 640–645. doi:10.1038/nmat4879.
[56] L. Ma, P. Priya, N.R. Aluru, A Multiscale Model for Electrochemical Reactions in LSCF Based Solid Oxide Cells, J. Electrochem. Soc. 165 (2018) F1232–F1241. doi:10.1149/2.0921814jes.
[57] N. Ai, S. He, N. Li, Q. Zhang, W.D.A. Rickard, K. Chen, T. Zhang, S.P. Jiang, Suppressed Sr segregation and performance of directly assembled La0.6Sr0.4Co0.2Fe0.8O3-δ oxygen electrode on Y2O3-ZrO2 electrolyte of solid oxide electrolysis cells, J. Power Sources. 384 (2018) 125–135. doi:10.1016/j.jpowsour.2018.02.082.
[58] S.P. Jiang, X. Chen, Chromium deposition and poisoning of cathodes of solid oxide fuel cells - A review, Int. J. Hydrogen Energy. (2014). doi:10.1016/j.ijhydene.2013.10.042.
[59] E.D. Wachsman, D. Oh, E. Armstrong, D.W. Jung, C. Kan, Mechanistic Understanding of Cr Poisoning on La, in: ECS Trans., ECS, 2009: pp. 2871–2879. doi:10.1149/1.3205852.
[60] A. Beez, K. Schiemann, N.H. Menzler, M. Bram, Accelerated Testing of Chromium Poisoning of Sr-Containing Mixed Conducting Solid Oxide Cell Air Electrodes, Front. Energy Res. 6 (2018). doi:10.3389/fenrg.2018.00070.
[61] B. Wei, K. Chen, C.C. Wang, Z. Lü, S.P. Jiang, Cr deposition on porous La0.6Sr0.4Co0.2Fe0.8O3−δ electrodes of solid oxide cells under open circuit condition, Solid State Ionics. 281 (2015) 29–37. doi:10.1016/j.ssi.2015.08.018.
[62] C. Graves, S.D. Ebbesen, S.H. Jensen, S.B. Simonsen, M.B. Mogensen, Eliminating degradation in solid oxide electrochemical cells by reversible operation, Nat Mater. 14 (2015) 239–244. doi:10.1038/nmat4165.
[63] D. Errandonea, A. Muñoz, P. Rodríguez-Hernández, J.E. Proctor, F. Sapiña, M. Bettinelli, Theoretical and Experimental Study of the Crystal Structures, Lattice Vibrations, and Band Structures of Monazite-Type $PbCrO_4$, $PbSeO_4$, $SrCrO_4$, and $SrSeO_4$, Inorg. Chem. 54 (2015) 7524–7535. doi:10.1021/acs.inorgchem.5b01135.
[64] G. Cappellini, S. Bouette-Russo, B. Amadon, C. Noguera, F. Finocchi, Structural properties and quasiparticle energies of cubic SrO, MgO and $SrTiO_3$, J. Phys. Condens. Matter. 12 (2000) 3671–3688. doi:10.1088/0953-8984/12/15/315.
[65] M.A. Hakeem, D.E. Jackson, J.J. Hamlin, D. Errandonea, J.E. Proctor, M. Bettinelli, High pressure raman, optical absorption, and resistivity study of SrCrO4, Inorg. Chem. 57 (2018) 7550–7557. doi:10.1021/acs.inorgchem.8b00268.